

## Modeling of the sheath and the energy distribution of ions bombarding rf-biased substrates in high density plasma reactors and comparison to experimental measurements

Erik A. Edelberg and Eray S. Aydil

Citation: *Journal of Applied Physics* **86**, 4799 (1999); doi: 10.1063/1.371446

View online: <http://dx.doi.org/10.1063/1.371446>

View Table of Contents: <http://scitation.aip.org/content/aip/journal/jap/86/9?ver=pdfcov>

Published by the *AIP Publishing*

---

### Articles you may be interested in

[Local retarding field for ions towards a positively biased substrate in plasma and its application to soft ion-bombardment processing](#)

*J. Appl. Phys.* **101**, 013302 (2007); 10.1063/1.2402972

[Effects of wafer impedance on the monitoring and control of ion energy in plasma reactors](#)

*J. Appl. Phys.* **100**, 063310 (2006); 10.1063/1.2353203

[Experimental and theoretical study of ion distributions near 300  \$\mu\text{m}\$  tall steps on rf-biased wafers in high density plasmas](#)

*J. Vac. Sci. Technol. A* **21**, 147 (2003); 10.1116/1.1527951

[Plasma etch/deposition modeling: A new dynamically coupled multiscale code and comparison with experiment](#)

*J. Vac. Sci. Technol. A* **18**, 2045 (2000); 10.1116/1.1285990

[Ion energy distributions and sheath voltages in a radio-frequency-biased, inductively coupled, high-density plasma reactor](#)

*J. Appl. Phys.* **85**, 3966 (1999); 10.1063/1.370298

---



# Modeling of the sheath and the energy distribution of ions bombarding rf-biased substrates in high density plasma reactors and comparison to experimental measurements

Erik A. Edelberg and Eray S. Aydil<sup>a)</sup>

*Department of Chemical Engineering, University of California–Santa Barbara, Santa Barbara, California 93106*

(Received 26 March 1999; accepted for publication 30 July 1999)

In plasma etching and deposition processes, the energy distribution of ions incident onto the substrate strongly affects the surface reactions and the film deposition and etching rates. The magnitude and frequency of the rf-bias power applied to the substrate electrode determines the spatiotemporal variations of the sheath potentials and hence the energy distribution of the ions impinging upon the substrate. A self-consistent dynamic model of the sheath, capable of predicting ion energy distributions impinging on a rf-biased electrode, was developed. The model consists of equations describing the charge transport in the sheath coupled to an equivalent circuit model of the sheath to predict the spatiotemporal charge and potential distributions near the surface. Experimental measurements of the energy distributions of ions impinging on a rf-biased electrostatic chuck have also been made in a high density transformer coupled plasma reactor through Ar and Ne plasmas. The predicted ion energy distributions and sheath profiles are in very good agreement with the experimental measurements. © 1999 American Institute of Physics. [S0021-8979(99)06321-5]

## I. INTRODUCTION

Low pressure, high density plasmas are commonly used in the microelectronics industry to etch thin films of metals, dielectrics, and semiconducting materials. In particular, inductively coupled plasmas (ICPs) excited by radio frequency (rf) fields generated by various different coil geometries have emerged as the preferred method for producing high ion densities ( $10^{11}$ – $10^{12}$  cm<sup>-3</sup>).<sup>1,2</sup> The ions play a crucial role in the etching of thin films and substrates as they impinge on the surface with energies ranging from tens to hundreds of electron volts. The ions gain this energy from the strong electric fields that exist near the surface as they travel from the plasma across the sheath towards the substrate. The potential drop from the plasma to the substrate electrode, the sheath potential, accelerates the ions created in the plasma towards the substrate. The electrode that the substrate is placed upon is often independently rf biased to increase the electric fields within the sheath and to control the energies of the ions impinging on the surface of the film to be etched. The ions strike the substrate surface with high energy and momentum concentrated primarily in the direction normal to the surface. The angular distribution of the ion velocities around the surface normal is affected by the magnitude of the sheath potential drop, the velocity distribution of ions at the sheath edge, and the collisions they undergo in the sheath. Knowledge of the angular distribution is essential for calculating etching profiles. The energy distribution of ions incident onto the substrate strongly affects the surface reactions and film etching rates.<sup>3</sup> The exact details of the spatial and temporal

variations of the electric fields within the sheath and the time dependence of the sheath thickness determine the energy distribution of the ions impinging on the surface. In order to accurately predict the ion energy distribution (IED), a self-consistent model of the sheath dynamics is needed.

Although there are limited direct comparisons of measured IEDs with predicted IEDs in ICP reactors, ion transport and radio frequency sheath dynamics have been investigated and modeled extensively, particularly in diode type reactors.<sup>4–21</sup> Most researchers focused on studying the spatial and temporal variation of the potential field within the sheath without calculating IEDs. However the calculated fields can be used to generate ion energy distributions. For example, Economou *et al.*<sup>5</sup> derived an analytical solution for the sheath potential for a time averaged sheath and investigated the effects of ion collisions within the sheath using this model. Lieberman<sup>6,7</sup> also derived analytical solutions describing the time averaged rf plasma sheath and investigated the sheath electrical characteristics assuming a sinusoidal current source. Sternberg and Godyak and Lieberman have done extensive modeling of collisional and collisionless capacitive sheaths.<sup>6–9,11,12</sup> Most recently Miller and Riley did an extensive study of collisionless rf plasma sheaths using a detailed equivalent circuit model of a specific experimental system which was used for comparing predicted voltage and current wave forms to the measured ones.<sup>14</sup>

Ion energy distributions across rf-biased sheaths have been modeled by several researchers.<sup>4,13,15,17–22</sup> As early as 1967, Tsui modeled the dependence of IEDs on the rf frequency assuming a collisionless sheath with a linear electric field and Maxwell–Boltzmann energy distributions for both

<sup>a)</sup>Corresponding author; electronic mail: aydil@engineering.ucsb.edu

ions and electrons in the plasma.<sup>15</sup> Around the same time, Benoit-Cattin and Bernard did an in depth study of the shape of IEDs in high frequency plasmas.<sup>22</sup> Metze *et al.* calculated the potential wave forms across a collisionless sheath through an equivalent circuit model in a capacitive parallel plate reactor, and determined the ion energy distribution functions.<sup>4,19</sup> Barnes *et al.* used Monte Carlo simulations of the ion trajectories in rf modulated sheaths to study the effects of the modulation frequency on the IEDs.<sup>20</sup> Kushner and Hebner and Kushner assumed a sinusoidal potential wave form across a rf-biased sheath and calculated substrate ion energies and angular distributions in capacitively coupled plasma reactors using Monte Carlo techniques to model the ion trajectories.<sup>17,18</sup> Kushner and co-workers also modeled the sheath and the IEDs in ICP reactors using a multimodule hybrid particle-fluid model.<sup>13,21</sup> In all of these studies, bimodal ion energy distributions were predicted for rf sheaths when the period of the rf bias is equal to or much longer than the average time it takes an ion to cross the sheath. Only at frequencies where the rf period is significantly shorter ( $\sim 10\times$ ) than the ion transit time did the bimodal distributions collapse to single peaked distributions at an energy corresponding to the time-averaged potential difference between the plasma and the electrode.

Ion energy and angle distribution functions have also been studied experimentally and measured in various types of plasma reactors. These measurements were reviewed in Refs. 23 and 24.

In this article, the results of a self-consistent dynamic model of the sheath, capable of predicting the ion energy distributions impinging on a rf-biased electrode are presented. The time dependent voltage wave form and sheath thickness as well as the spatially and temporally varying electric field, drift velocity, and charge densities are calculated and shown for various rf-bias powers, bulk plasma ion densities, and electron temperatures. Using the calculated fields, ion energy distributions bombarding a rf-biased electrode are determined through Monte Carlo simulations of the ion trajectories. These results are compared to the energy distributions of ions impinging on a rf-biased electrostatic chuck in a transformer coupled plasma (TCP) reactor measured with a recently developed floating ion energy analyzer.<sup>23,24</sup> Model predictions are compared to the experimental measurements in Ar and Ne plasmas over a wide range of TCP powers, rf-bias powers, and gas pressure values.

## II. MODEL DESCRIPTION

A model that is capable of predicting the energy distribution function of ions bombarding a rf-biased electrode surface as a function of plasma operating conditions must be able to account for the spatiotemporal variation of the electric field and the potential distribution that accelerates the ions in the sheath. Since the electric field profiles depend on the charge distribution in the sheath, the model must also take into account the ion and electron density variations as a function of time and position. Thus, the equations that describe electron and ion transport are coupled to Poisson's

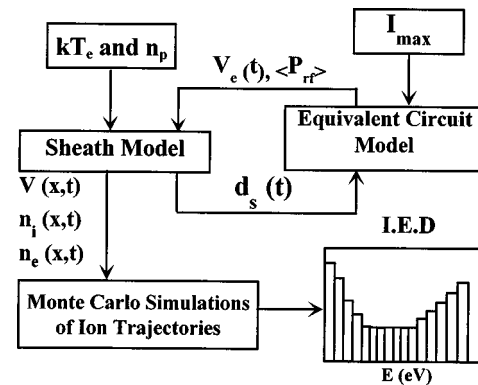


FIG. 1. Flow chart of the model used for predicting energy distributions of ions impinging on a rf-biased electrode. The flow chart shows the coupling between the sheath model, the equivalent circuit model, and the Monte Carlo simulations of ion trajectories.

equation which must be solved simultaneously and self-consistently for the charge and electric field distributions. Once the spatiotemporal variation of the electric field that accelerates the ions is known, the ion energy distribution function can be calculated either numerically or by Monte Carlo simulation methods.

The model described herein consists of three coupled modules, which are illustrated in Fig. 1. The “sheath module” is used to calculate the spatiotemporal variation of the electric field, the sheath potential, the sheath thickness, the ion drift velocity, and the ion and electron concentrations given the time variation of the spatially integrated sheath potential across the sheath. A nonlinear equivalent circuit model of the sheath is the second module and it is used to calculate the spatially integrated sheath potential wave form consistent with the given bias power and the sheath thickness as calculated in the sheath module. The final module is a Monte Carlo simulation which is used to compute the ion trajectories as they are accelerated by the electric fields that are calculated self-consistently using the sheath and the equivalent circuit models. In the following we describe each module in detail and the assumptions used in developing the model.

### A. Sheath model

#### 1. Model equations

We consider the sheath near a rf-biased electrode in a low pressure regime where collisions in the sheath may be neglected. The sheath thicknesses calculated using the model were typically several hundred microns, much less than the mean free path of ions and neutrals which is several millimeters at 10 mTorr. We assume that the sheath is infinite in the direction parallel to the electrode surface. The model geometry and coordinate system are shown in Fig. 2. The one-dimensional spatiotemporal variation of the ion density,  $n_i(x,t)$ , the ion drift velocity,  $u_i(x,t)$ , and the electric potential,  $V(x,t)$  are described by the ion continuity equation,

$$\frac{\partial n_i}{\partial t} + \frac{\partial}{\partial x}(u_i n_i) = 0, \quad (1)$$

the ion momentum balance,

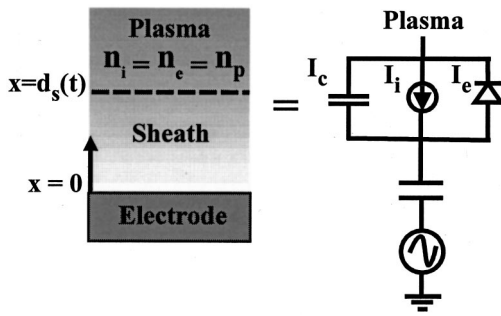


FIG. 2. Model geometry and the equivalent circuit used to model the sheath.

$$\frac{\partial u_i}{\partial t} + u_i \frac{\partial u_i}{\partial x} = -\frac{e}{m_i} \frac{\partial V}{\partial x}, \quad (2)$$

and the Poisson's equation,

$$\frac{\partial^2 V}{\partial x^2} = -\frac{e}{\epsilon_0} (n_i - n_e). \quad (3)$$

In Eqs. (1)–(3)  $e$  is the electronic charge,  $\epsilon_0$  is the permittivity of free space, and  $m_i$  is the ion mass. The three equations are not only coupled to each other but also to the electron density,  $n_e$ . We assume that the energy distribution of the electrons in the plasma is given by a Maxwell–Boltzmann distribution and characterized by an electron temperature,  $T_e$ . Furthermore, we limit ourselves to bias frequencies in the radio frequency range and well below the electron plasma frequency such that the electrons respond to the changes in the potential instantaneously. This is typically the case in plasma etching and deposition reactors where the bias frequencies are in the 0.1–20 MHz range. With these assumptions and taking the potential at the plasma–sheath edge to be zero, the reference potential, the electron density as a function of position in the sheath is given by

$$n_e(x, t) = n_p \exp\left(\frac{eV(x, t)}{kT_e}\right), \quad (4)$$

where  $n_p$  is the electron density at the plasma–sheath boundary and  $k$  is the Boltzmann's constant.

Suitable boundary conditions at the plasma–sheath interface must be chosen to completely define the problem. Artificial delineation of the sheath from the plasma forces one to define the sheath–plasma boundary. In this model we define the sheath boundary as suggested by Economou *et al.*<sup>5</sup> which is similar to an earlier treatment given by Godyak and Sternberg.<sup>9</sup> We take the plasma–sheath interface as the point at which the electric field has increased to  $kT_e/2e\lambda_D$  where  $\lambda_D = (\epsilon_0 kT_e/n_p e^2)^{1/2}$  is the Debye length. This is the field required to accelerate the ions to the Bohm velocity across a distance equal to one Debye length. In terms of the potential this boundary condition may be written as

$$\frac{\partial V}{\partial x} = \frac{kT_e}{2e\lambda_D}, \quad \text{at } x = d_s(t), \quad (5)$$

where  $d_s(t)$  is the time dependent sheath thickness. Since potential reference can be taken arbitrarily, we set

$$V = 0, \quad \text{at } x = d_s(t), \quad (6)$$

and take the value of potential at the electrode to be

$$V = V_e(t), \quad \text{at } x = 0. \quad (7)$$

$V_e(t)$  is obtained by coupling this model to an equivalent circuit model of the sheath as is close in Sec. II B. We note that only two boundary conditions are needed to solve for  $V(x, t)$ ; the third boundary condition defines the location of the sheath,  $d_s(t)$ , as a function of time. Consistent with boundary condition (5), we assume that the ions enter the sheath with a velocity equal to the Bohm velocity and use

$$u_B = \sqrt{\frac{kT_e}{m_i}}, \quad \text{at } x = d_s(t) \quad (8)$$

as a boundary condition for the ion velocity. Finally, we assume that the ion density at the plasma–sheath edge is known:

$$n = n_p, \quad \text{at } x = d_s(t). \quad (9)$$

A bulk plasma model would normally provide the concentration at this location and the two solutions would be matched at the plasma–sheath interface.

## 2. Dimensional analysis

Here in Sec. II A2 we nondimensionalize Eqs. (1)–(3) in order to examine the relative contributions from the different terms in Eqs. (1)–(3). The variables in these equations are nondimensionalized using characteristic voltage, distance, and time such that the magnitude of the dimensionless solution is of order one in a major portion of the domain,  $0 < x < d_s(t)$ . Specifically, we set

$$\tilde{t} = ft, \quad \tilde{x} = \frac{x}{d_{CLS}}, \quad \tilde{V} = \frac{V}{V_{\max}}, \quad \tilde{u}_i = \frac{u_i}{u_{i\max}}, \quad \tilde{n}_i = \frac{n_i}{n_p}, \quad (10)$$

where the quantities with (‘‘~’’) are the dimensionless variables,  $V_{\max}$  is the maximum potential drop across the sheath, and  $u_{i\max} = (2eV_{\max}/m_i)^{1/2}$  is the maximum velocity that an ion would reach after falling through that potential. Time is nondimensionalized using the period corresponding to the applied frequency,  $f$ . The position variable is made dimensionless using a sheath thickness,  $d_{CLS}$ , given by Child–Langmuir law,

$$d_{CLS} = \frac{2}{3} \sqrt{\epsilon_0} \left( \frac{2e}{m_i} \right)^{1/4} \frac{V_{\max}^{3/4}}{J_i^{1/2}}, \quad (11)$$

corresponding to a dc sheath with a potential drop of  $V_{\max}$  and ion current density given by

$$J_i = eu_B n_p. \quad (12)$$

The dimensionless continuity, momentum balance, and Poisson's equation become

$$\beta \frac{\partial \tilde{n}_i}{\partial \tilde{t}} + \frac{\partial}{\partial \tilde{x}} (\tilde{n}_i \tilde{u}_i) = 0, \quad (13)$$

$$\beta \frac{\partial \tilde{u}_i}{\partial \tilde{t}} + \tilde{u}_i \frac{\partial \tilde{u}_i}{\partial \tilde{x}} = -\frac{1}{2} \frac{\partial \tilde{V}}{\partial \tilde{x}}, \quad (14)$$

$$\frac{\partial^2 \tilde{V}}{\partial \tilde{x}^2} = -\frac{4}{9} \phi_{\max} (\tilde{n}_i - e^{\phi_{\max} \tilde{V}}), \quad (15)$$



where

$$\phi_{\max} = \frac{eV_{\max}}{kT_e}, \quad (16)$$

and

$$\beta = \frac{1}{3\pi} \left( \frac{f}{f_{ip}} \right) \left( \frac{\phi_{\max}}{2} \right)^{1/4}. \quad (17)$$

In Eq. (17),  $f_{ip}$  is the ion plasma frequency given by

$$f_{ip} = \frac{1}{2\pi} \left( \frac{e^2 n_p}{\epsilon_0 m_i} \right)^{1/2}. \quad (18)$$

The dimensionless parameter  $\beta$  in Eqs. (13) and (14) determines whether the term involving the time derivative is important for the solution of the set of equations that describes the time and position dependence of the ion density, the velocity, and the potential. When  $\beta \ll 1$  the time derivative term can be neglected even though the ion density and velocity may still be functions of time. In this case the ion density and velocity are said to follow the time variations in the sheath. For example, for an Ar plasma with  $f = 4$  MHz,  $n_p = 10^{11} \text{ cm}^{-3}$ ,  $V_{\max} = 200$  V, and  $kT_e = 3$  eV,  $\beta$  is 0.1. For the parameter values of interest in this article,  $\beta$  is typically less than 0.1 and the time derivative term is negligible. Thus, in order to calculate the potential we assume that the ion density and velocity follow the temporal variation of the field and neglect the time dependent terms in Eqs. (13) and (14). The most important result of the sheath model for the ion energy distribution function calculations is the spatiotemporal variation of the potential in the sheath. While the potential depends on the charge density, it is relatively insensitive to details of the variation of the ion density and velocity with time. However the fact that individual ions cannot respond to the field instantaneously will be taken into account in the Monte Carlo simulations.

We also note that in most discussions of the temporal response of ions in the sheath, the applied frequency,  $f$ , is compared to the ion plasma frequency,  $f_{ip}$ . For example if  $f \ll f_{ip}$ , ions are assumed to respond to the field instantaneously whereas when  $f \gg f_{ip}$ , they are assumed to respond to a time-averaged field. The above analysis shows that, for the purposes of calculating the spatiotemporal variation of the ion density and the average drift velocity, the relevant time scale is the ion transit frequency, which is the reciprocal of the time required for an ion to cross the sheath. Note that  $\beta$  can be small and the time derivatives can be neglected even when the applied frequency is close to the ion plasma frequency.

While the scaling analysis above is useful for discussing the relative magnitudes of the terms that contribute to the ion continuity and momentum balance equations, the dimensionless variables are inconvenient for solving the problem. For example, since the integrated potential wave form is not yet determined, the maximum potential and the maximum velocities are not known. Thus, for convenience, before solving Eqs. (1)–(3) we nondimensionalize again, this time using the Debye length,  $\lambda_D$ , the Bohm velocity,  $u_B$ , and the electron

temperature,  $kT_e/e$ , to nondimensionalize the position, the ion velocity, and the potential, respectively. Using the new dimensionless variables,

$$\zeta = \frac{x}{\lambda_D}, \quad \tau = ft, \quad \phi = \frac{eV}{kT_e}, \quad \theta_i = \frac{n_i}{n_p}, \quad v_i = \frac{u_i}{u_B}, \quad (19)$$

Eqs. (1)–(3) become

$$\frac{\partial}{\partial \zeta} (\theta_i v_i) = 0, \quad (20)$$

$$v_i \frac{\partial v_i}{\partial \zeta} = - \frac{\partial \phi}{\partial \zeta}, \quad (21)$$

and

$$\frac{\partial^2 \phi}{\partial \zeta^2} = (e^\phi - \theta_i). \quad (22)$$

The dimensionless boundary conditions become

$$\theta_i = 1 \quad \text{at } \zeta = s(\tau), \quad (23)$$

$$v_i = 1 \quad \text{at } \zeta = s(\tau), \quad (24)$$

$$\frac{\partial \phi}{\partial \zeta} = \frac{1}{2} \quad \text{at } \zeta = s(\tau), \quad (25)$$

$$\phi = 0 \quad \text{at } \zeta = s(\tau), \quad (26)$$

and

$$\phi = \phi_e(\tau) \quad \text{at } \zeta = 0, \quad (27)$$

where  $s(\tau) = d_s(t)/\lambda_D$  is the time dependent sheath thickness and  $\phi_e(\tau)$  is the dimensionless spatially integrated potential drop from the plasma–sheath interface to the electrode.

Equations (20) and (21) are integrated to give the ion density,

$$\theta_i = \frac{1}{\sqrt{1 - 2\phi}}, \quad (28)$$

and the velocity,

$$v_i = \sqrt{1 - 2\phi}, \quad (29)$$

as a function of the dimensionless potential. Substitution of the ion density into the dimensionless Poisson equation and integration using boundary condition (25) yields

$$\frac{\partial \phi}{\partial \zeta} = \left[ 2(\sqrt{1 - 2\phi} + e^\phi) - \frac{15}{4} \right]^{1/2}, \quad (30)$$

for the dimensionless field. Equation (30) is integrated numerically using a fourth-order Runge–Kutta method over the interval  $0 \leq \phi \leq \phi_e(\tau)$  to give the spatially resolved time dependent potential drop across the sheath,  $V(x, t)$ , and the time dependent sheath thickness,  $d_s(t)$ .  $V_e(t)$  and thus  $\phi_e(t)$  is obtained by solving a nonlinear equivalent circuit model of the sheath which will be described next.

## B. Equivalent circuit model of the sheath

With a few exceptions,<sup>14,19</sup> previous models assumed that the potential drop across the sheath is either linear in

space or purely sinusoidal in time. The precise spatiotemporal variation of the potential drop across the sheath is essential for the successful prediction of the distribution of ion energies bombarding the rf-biased electrode. In order to calculate the time variation of the potential drop from the plasma to the electrode, the sheath is modeled as a parallel combination of a diode, a capacitor, and a current source as shown in Fig. 2. The current through the diode represents the variation of the electron current as a function of the sheath potential drop,  $V_s(t) = V_p - V_e(t) = -V_e(t)$ , and the  $I$ - $V$  characteristics of the diode are given by

$$I_e = \frac{eu_en_p A}{4} \exp\left(\frac{eV_s(t)}{kT_e}\right), \quad (31)$$

where  $A$  is the electrode area and  $u_e = (8kT_e/\pi m_e)^{1/2}$  is the mean velocity of an electron with mass  $m_e$ . The current source represents the current due to ions with mass  $m_i$  that enter the sheath from the plasma-sheath boundary at the Bohm velocity. Accordingly, the total ion current is taken to be

$$I_i = eAu_B n_p. \quad (32)$$

The capacitive displacement current,  $I_d$ , can be derived as

$$I_d \equiv \frac{dQ}{dt} = \frac{dQ}{dV_e} \frac{dV_e}{dt} \equiv C_s(t) \frac{dV_e}{dt}, \quad (33)$$

where  $C_s(t)$  is the time dependent sheath capacitance given by

$$C_s(t) = \frac{\epsilon_0 A}{d_s(t)}. \quad (34)$$

Assuming that the current at the electrode from the rf-bias supply is sinusoidal, a current balance at the electrode yields

$$I_i - I_e - C_s(t) \frac{dV_e(t)}{dt} = I_{\max} \sin(2\pi ft). \quad (35)$$

The current balance is coupled to the sheath model through the electrode potential  $V_e(t)$  and the sheath thickness  $d_s(t)$ . Thus Eq. (35) must be solved simultaneously with the sheath equations described in Sec. II A. For an initial guess of  $d_s(t)$ , Eq. (35) is integrated assuming constant sheath capacitance and using the fourth-order Runge-Kutta method to obtain the potential drop across the sheath. Using this potential wave form in the sheath model, a new  $d_s(t)$  is calculated and the iteration is repeated until the potential and the sheath thickness as a function of time converge to a self-consistent periodic steady state solution. The rf-bias power to the electrode is calculated from the time dependent voltage and current wave forms such that

$$\langle P_{\text{rf}} \rangle = \frac{1}{\tau} \int_0^\tau V_s(t) I(t) dt, \quad (36)$$

where  $I(t) = I_{\max} \sin(2\pi ft)$ .

### C. Monte Carlo model of the ion transport across the sheath

The simultaneous solution of the sheath model with the equivalent circuit model yields the spatiotemporal variation

of the potential and the electric field in the sheath. This electric field is used in a Monte Carlo model of the collisionless ion transport across the sheath to determine the distribution of ion energies striking the electrode. The ions are injected into the sheath from the sheath edge,  $x = d_s(t)$ , at different times during a cycle. The ions are given random velocities,  $u_i = u_B \pm u_{\text{ith}}$ , where  $u_{\text{ith}}$  is the thermal component of the ion's velocity at the sheath edge, picked randomly from a Boltzmann velocity distribution with temperature  $kT_+$ , where the ion temperature,  $T_+$ , is assumed to be 500 K. The equation of motion for the ions,

$$m_i \frac{d^2 x(t)}{dt^2} = eE(x, t), \quad (37)$$

is integrated and the ion velocity and position are followed as they travel towards the electrode. In Eq. (37),  $E(x, t)$  is the electric field calculated from the simultaneous solution of the sheath and the equivalent circuit models. When the ion reaches the electrode, its energy is calculated and recorded in a histogram of energies with bin size  $\Delta E$ . For comparison with experimentally measured IEDs, the bin size  $\Delta E$  was chosen to be 3 eV which is the approximate resolution of the ion energy analyzer used for the experimental measurements.

Although we have not done so, angular distributions of ions striking the wafer surface can also be calculated using this model and the methodology described by Gottscho.<sup>25</sup> However, calculation of the angular distributions requires knowledge of the isotropic component of the velocity distribution function (e.g., ion temperature) at the plasma-sheath interface. In the Monte Carlo simulations, the ion incidence angle distribution,  $f(\theta)$ , can be calculated using

$$f(\theta) = C_N \exp\left(-\frac{E}{kT_+} \theta^2\right), \quad (38)$$

where  $C_N$  is the normalization constant,  $E$  is the ion energy,  $k$  is the Boltzmann's constant, and  $T_+$  is the ion temperature.

## III. EXPERIMENT

A compact floating ion energy analyzer capable of measuring the energy distribution of ions impinging on a rf-biased electrostatic chuck in an inductively coupled plasma reactor has been designed and built.<sup>23,24</sup> The retarding field analyzer is designed to operate while embedded in the electrostatic chuck of a Lam TCP reactor as shown in Fig. 3. The analyzer electronics have been designed to operate while floating on several hundred volts of rf bias while accurately measuring small dc voltages and currents. Optical fibers are used to communicate voltage setpoints and current monitoring data to and from the floating electronics of the analyzer to the computer used for data acquisition in the experiments. In order to minimize the modifications to the Lam reactor and to avoid differential pumping of the analyzer, the analyzer was made to be compact, with critical dimensions less than the mean free path of ions at the operating pressures of interest for this work. Details of the analyzer design and the analyzer electronics are discussed elsewhere.<sup>23,24</sup>

Figure 3 shows the high density Lam TCP reactor with several diagnostics including the ion energy analyzer and

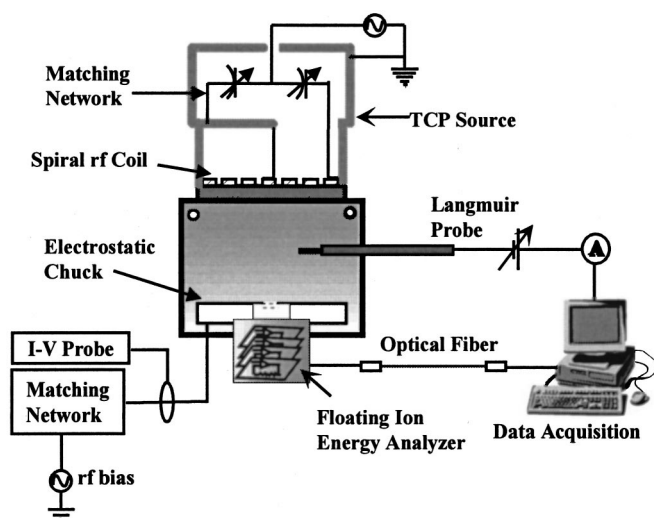


FIG. 3. Experimental setup showing the various plasma diagnostics and the floating retarding grid energy analyzer used to measure the energy distributions of ions impinging on the rf-biased electrostatic chuck in a Lam TCP reactor.

accompanying electronics built into the electrostatic chuck. The plasma is excited by a planar coil that sits above a quartz window on top of the reactor and is powered by 13.56 MHz rf power supply at 200–2000 W. Gases are injected through a gas dispersion ring near the quartz window. A manifold of gas flow controllers controls the flow rate of the gases, which are removed from the reactor by a 2000  $\ell$ /s turbomolecular pump. The pressure in the reactor is set by controlling a throttle valve located directly above the pump and is typically maintained between 2 and 30 mTorr. The electrostatic chuck is located 10 cm below the quartz window and independently biased by a 4 MHz rf power supply at powers up to 800 W. A current–voltage probe is used to measure the time-averaged power, root mean square (rms) voltage, and current delivered to the chuck while the voltage wave forms on the chuck are measured using a high impedance voltage probe. A Langmuir probe inserted into the center of the reactor is used to measure the average ion and electron densities as well as the plasma and floating potentials.

#### IV. RESULTS AND DISCUSSION

##### A. Modeling results

We now present results from the sheath and equivalent circuit simulation modules to gain insight into the sheath dynamics and to see how the ion energy distribution is affected by plasma parameters such as the ion density,  $n_i$ , (i.e., TCP coil power), electron temperature,  $kT_e$ , rf-bias frequency,  $f$ , and rf-bias power,  $P_{rf}$ . The model requires the ion and electron density at the plasma–sheath interface, the electron temperature, rf-bias frequency, and the peak current as inputs. The peak current determines the total rf-bias power and may be viewed as the rf-bias power parameter. To explore the effects of the input parameters on the model, we varied each parameter one by one while keeping the others constant at a typical base value. For the simulation results presented herein we used typical conditions in the TCP re-

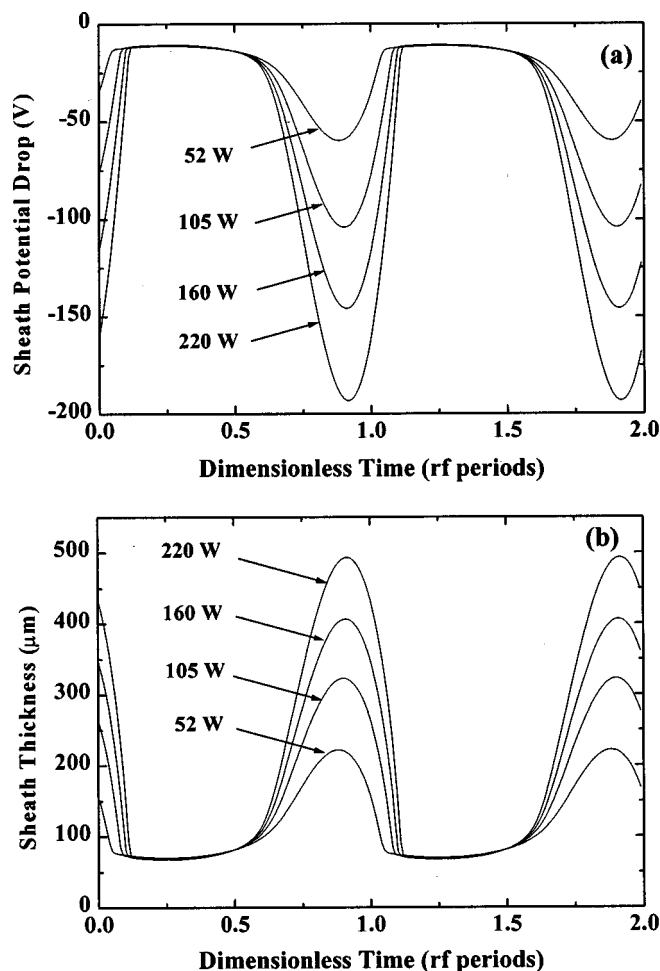


FIG. 4. (a) Spatially integrated sheath voltage wave form and (b) the time dependent sheath thickness calculated from the sheath model for an Ar plasma for several rf-bias powers. The bias frequency, the ion density, and the electron temperature were fixed at 4 MHz,  $3 \times 10^{11} \text{ cm}^{-3}$ , and 3 eV, respectively.

actor with argon as the feed gas. The base values of the input parameters were  $n_i = 3 \times 10^{11} \text{ cm}^{-3}$ ,  $kT_e = 3 \text{ eV}$ ,  $f = 4 \text{ MHz}$ ,  $P_{rf} = 80 \text{ W}$ , and  $A = 325 \text{ cm}^2$  (8 in. wafer electrode area). Under these conditions the Debye length is 18  $\mu\text{m}$ .

Figures 4(a) and 4(b) show the voltage wave forms and the corresponding time dependent sheath thicknesses for several rf-bias power values ranging between 50 and 220 W. The bias power values are adjusted by changing the maximum total rf current,  $I_{\text{max}}$ . The voltage wave form has a large negative excursion for some part of the rf cycle, but remains close to the plasma potential for a significant fraction of the period. Integration of the Poisson equation from the electrode potential to the plasma potential yields the sheath thickness at each time in the rf cycle. Figure 4(b) shows the sheath thickness as a function of time for the same rf-bias powers that the voltage wave forms of Fig. 4(a) were calculated. As the potential wave form reaches its maximum voltage drop, the sheath thickness reaches its maximum thickness.

The voltage wave form on the electrode is dictated by the requirement that the time-averaged net current at the electrode must be zero. This wave form can be most easily

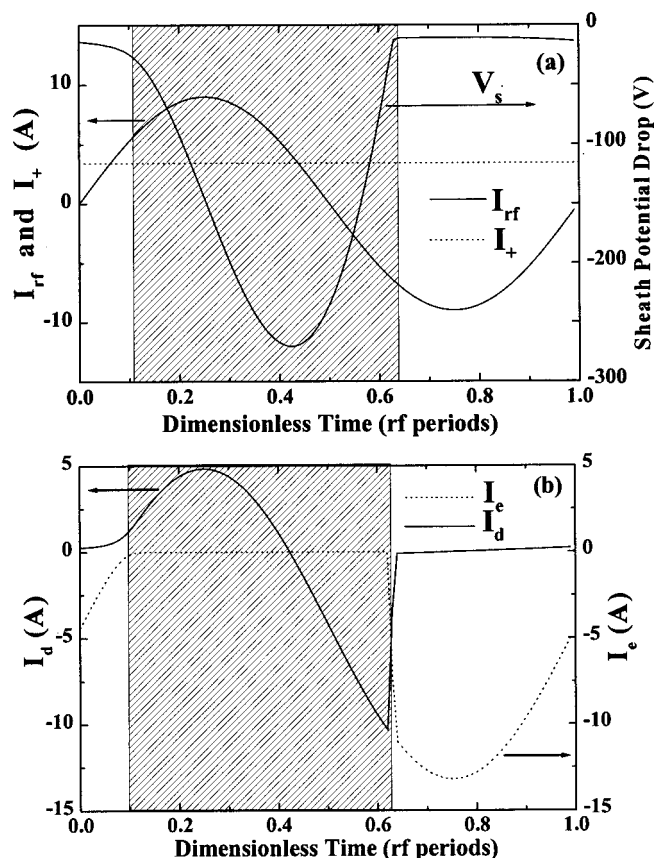


FIG. 5. Contributions to the total rf current at the electrode over one rf period. The rf supply current ( $I_{rf}$ ) is balanced by the ion current ( $I_+$ ), the electron current ( $I_e$ ), and the capacitive displacement current ( $I_d$ ).

understood by investigating the contributions from the electron, ion, and displacement currents,  $I_e$ ,  $I_+$ , and  $I_d$ , to the total current,  $I_{rf}$ , as a function of time. Figure 5 shows typical current wave forms for  $I_e$ ,  $I_d$ , and  $I_+$  and the total current,  $I_{rf}$  overlaid with the voltage wave form during one rf period. The ion current is constant and time independent, therefore the displacement current, the electron current, and the applied current will most strongly influence the voltage wave form. As the applied current to the electrode is driven positive, the balancing positive current is in part a result of the ions impinging on the electrode. The additional positive current, beyond that of the ion current, required to balance Eq. (35) is provided by the displacement current, which leads to the dramatic and rapid negative swing in the voltage. During the large negative excursion of the voltage from the plasma potential, the shaded region in Fig. 5, the sheath current balance is dominated by the displacement current. As the sheath potential drop increases, the sheath increases in thickness and the electrons are strongly repelled out of the sheath; the electron current in the shaded region in Fig. 5 is negligible. As the applied current begins to decrease below the ion current, the displacement current must become negative to satisfy the current balance since the potential at this point is still too high for electrons to reach the electrode and contribute to the balance. The displacement current becomes negative resulting in the derivative of the voltage with respect to time becoming positive which is manifested as the

minimum in the voltage wave form. The displacement current remains negative and decreases up to the point where the voltage difference between the plasma and the electrode drops enough to allow the electrons to reach the electrode to balance the ion current. When the electrons start flowing towards the electrode, the electron current increases exponentially and therefore rather abruptly. Due to this exponential dependence of the electron current on the sheath potential, only a slight change in the potential is required to allow enough electrons to the surface to satisfy the current balance. Thus, the potential remains relatively constant for this portion of the rf cycle. During the time that the electrode voltage is constant the displacement current is negligible and only the ion and the electron currents balance the rf driving current. The value of the voltage over this region is just slightly lower than the floating potential of the plasma. In this region the electrode behaves like a floating Langmuir probe. Since the floating potential is strictly a function of the electron temperature and the ion mass and does not depend on the rf-bias power, the most positive voltage of the wave form remains relatively constant and independent of the rf-bias power, as can be seen in Fig. 4(a). However, as the rf-bias power is increased, the peak-to-peak voltage appearing on the electrode increases.

Figures 6 and 7 show the spatially resolved sheath potential, ion drift velocity, and electron and ion densities for one of the wave forms (105 W) in Fig. 4 at four different times during one rf cycle. The potential profiles in Fig. 6(a) decrease from zero at the plasma-sheath interface to the instantaneous electrode potential. The distance from the electrode at which the potential equals zero is the sheath thickness at that time. The drift velocity [Fig. 6(b)] increases as the electric field in the sheath accelerates the ions towards the electrode. Figure 7 shows the spatiotemporal variation of the electron and ion densities in the sheath. The ion density decreases approximately an order of magnitude from that of the bulk plasma density at the plasma-sheath interface to the electrode. The drop in electron density is even steeper, dropping to zero within a few Debye lengths from the plasma-sheath interface. Electrons reach the electrode only when the sheath is thin and the sheath potential drop is small enough, on the order of a few  $kT_e$ . This corresponds to the flat regions of the potential wave forms shown in Fig. 4(a).

Figure 8 displays the ion energy distributions for the simulated sheath potentials and thicknesses shown in Fig. 4. A bimodal distribution with the majority of the ions arriving at low energies (10–20 eV) is predicted for low values of the rf-bias power. Bimodal distributions of the ion energy are expected when the ion transit time across the sheath is less than or on the order of the rf-bias period. Ions traversing the sheath during the period in the rf cycle where the potential drop across the sheath is small will arrive at the electrode with low energies and contribute to the low energy peak in the IED. In contrast, the ions entering and traversing the sheath during the period in the rf cycle where the potential drop across the sheath is large will arrive at the electrode with high energies and contribute to the high energy peak in



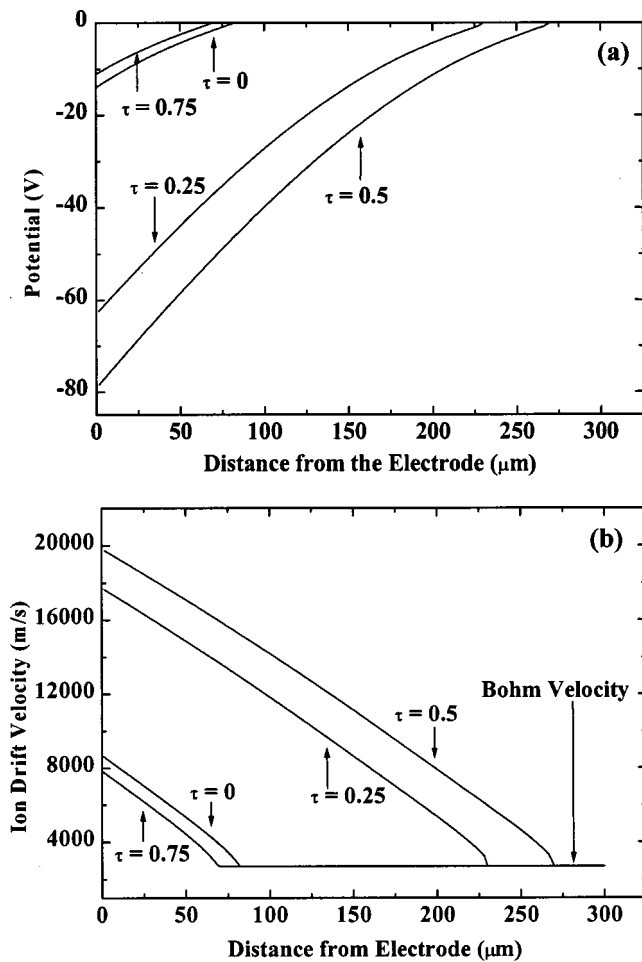


FIG. 6. Spatial dependence of (a) the sheath potential and (b) the average ion velocity in the sheath region of an Ar plasma at four different times during one rf cycle. The rf-bias frequency, the rf-bias power, the ion density, and the electron temperature were fixed at 4 MHz, 100 W,  $3 \times 10^{11} \text{ cm}^{-3}$ , and 3 eV, respectively.

the IED. As the rf-bias power is increased, the peak-to-peak voltage on the electrode also increases. This increase in voltage is manifested in the ion energy distribution as a shift of the high energy peak position to higher energies with increasing bias power. The effect of increasing the rf-bias power on the peak positions is illustrated in the inset of Fig. 8, which shows the positions of the low and high energy peaks in the bimodal IED as a function of the rf-bias power. The low energy peak position does not change significantly; however, the location of the high energy peak increases linearly as a function of the rf-bias power. As previously discussed, the most positive value of the voltage wave form is pinned close to the floating potential which remains approximately constant as a function of the rf-bias power, resulting in very weak dependence of the low energy peak position on the rf-bias power. Another notable affect of increasing the rf-bias power is the reduction in the low energy peak height. In contrast, the height of the high energy peak remains constant as the rf-bias power is increased. Thus, the ions that belonged to the low energy peak shift towards energies that are in between the two peaks. This shift can be understood by examining the temporal variation of the potential wave

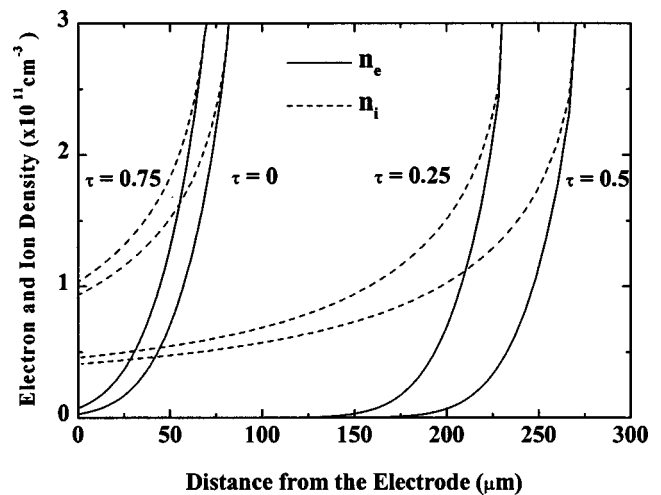


FIG. 7. Spatial dependence of the electron density,  $n_e$ , and the ion density,  $n_i$ , in the sheath region of an Ar plasma at four different times during one rf cycle. The rf-bias frequency, the rf-bias power, the plasma density, and the electron temperature were fixed at 4 MHz, 100 W,  $3 \times 10^{11} \text{ cm}^{-3}$ , and 3 eV, respectively.

form and the sheath thickness as a function of the rf-bias power. Two effects are responsible for the decrease in the low energy peak of the ion energy distribution function with increasing rf-bias power. First, as the rf-bias power increases, the fraction of the time that the potential is pinned near the floating potential decreases. In fact, the fraction of time the wave form spends at large negative excursions from the plasma potential increases. Second, the sheath thickness becomes so thick that ions that have entered the sheath when the wave form was close to the plasma potential are not accelerated to high enough velocities to traverse the sheath completely before the electrode potential changes. These ions will still be traversing the sheath when the potential drop from the plasma to the electrode becomes large and negative. Thus, they will be accelerated by larger electric fields and arrive at the electrode with higher energy than if

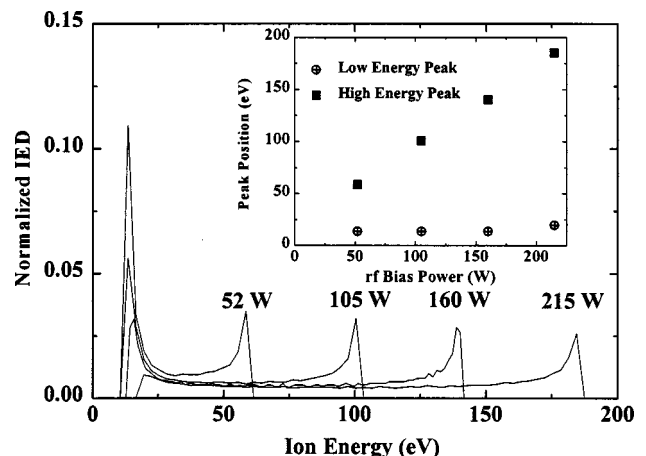


FIG. 8. Simulated ion energy distributions for an Ar plasma for several rf-bias powers. The corresponding sheath voltage and sheath thickness are shown in Fig. 4. The simulation parameters are the same as those in Fig. 4. The inset shows the position in energy of the high and low energy peaks of the bimodal distributions as a function of the rf-bias power.

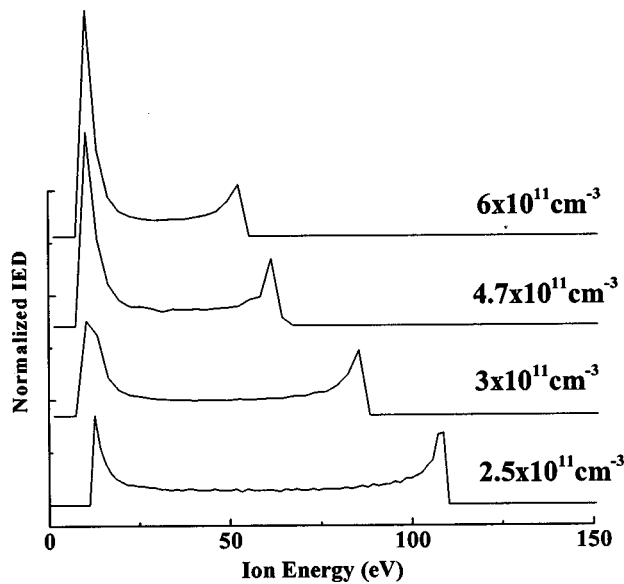


FIG. 9. Effect of the plasma ion density on the simulated ion energy distribution in an Ar plasma. The rf-bias frequency, power, and the electron temperature are fixed at 4 MHz, 80 W, and 3 eV, respectively. The distributions were shifted upward on the IED axis for clarity.

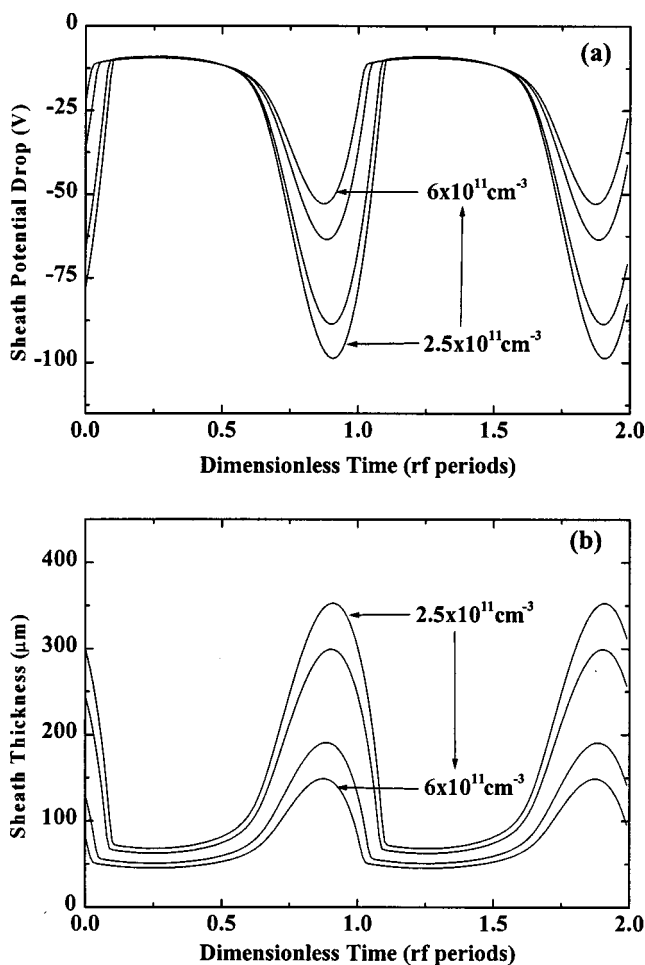


FIG. 10. Effect of the plasma ion density on the spatially integrated sheath potential wave form and the sheath thickness in an Ar plasma. The rf-bias frequency, power, and the electron temperature are fixed at 4 MHz, 80 W, and 3 eV, respectively. The direction of the arrow shows the trends in the wave forms as the ion density at the plasma-sheath interface is changed from  $2.5 \times 10^{11}$  to  $6 \times 10^{11} \text{ cm}^{-3}$ . The corresponding IEDs are shown in Fig. 9.

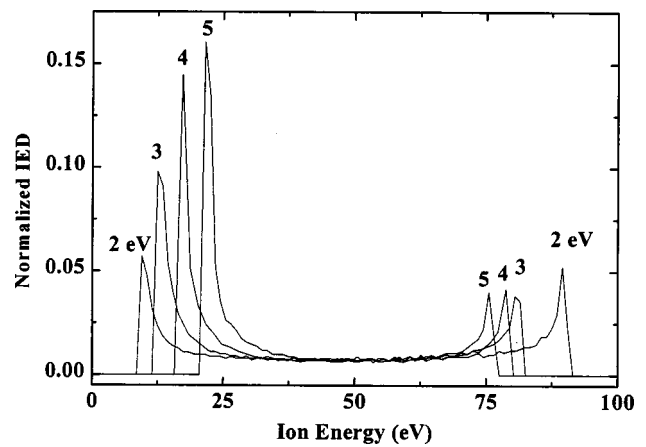


FIG. 11. Effect of the electron temperature on the simulated ion energy distribution in an Ar plasma. The rf-bias frequency, power, and the plasma ion density are fixed at 4 MHz, 80 W, and  $3 \times 10^{11} \text{ cm}^{-3}$ , respectively.

they were able to complete their flight across the sheath while the potential drop remained at its lowest.

Figure 9 shows the effect of the plasma ion density on the ion energy distributions while keeping the rf-bias power and the electron temperature at their base values. Increasing the ion density shifts the high energy peak position of the IED to lower energies. The effect of increasing the ion density on the voltage wave form and the sheath thickness is shown in Fig. 10. The peak-to-peak voltage decreases with increasing plasma ion density and this accounts for the high energy peak shift in the IED. As the ion current to the electrode increases as a result of higher plasma density, the voltage must decrease to maintain the same rf-bias power, resulting in smaller peak-to-peak sheath voltages. A more subtle effect of changing the ion density is the slight shift in the low energy peak position and the change in the low energy peak height. The low energy peak shifts slightly to lower energies and increases in height with increasing ion density despite the fact that the minimum sheath potential drop is independent of the ion density, pinned near the floating potential which depends only on the ion mass and electron temperature. Decreasing sheath thickness with increasing ion density, shown in Fig. 10(b), is responsible for the slight shift of the low energy peak to lower energies as well as the increase in the low energy peak height. This effect was discussed in some detail in reference to Fig. 8 in the previous paragraph.

Figure 11 shows the effects of changing the electron temperature on the simulated ion energy distributions in an Ar plasma with the ion density and rf-bias power held constant at their base values. The predominant effect of increasing the electron temperature is the decrease in energy separation between the low and high energy peaks of the distribution. The position of the low energy peak shifts to higher energies as the electron temperature is increased while the high energy peak shifts to lower energies. The shift in the low energy peak position is a result of an increase in the minimum potential difference,  $\Delta V_{s,\min}$ , between the plasma and the electrode. The value of this minimum potential difference is very close to the difference between the plasma and floating potentials for reasons explained previously.

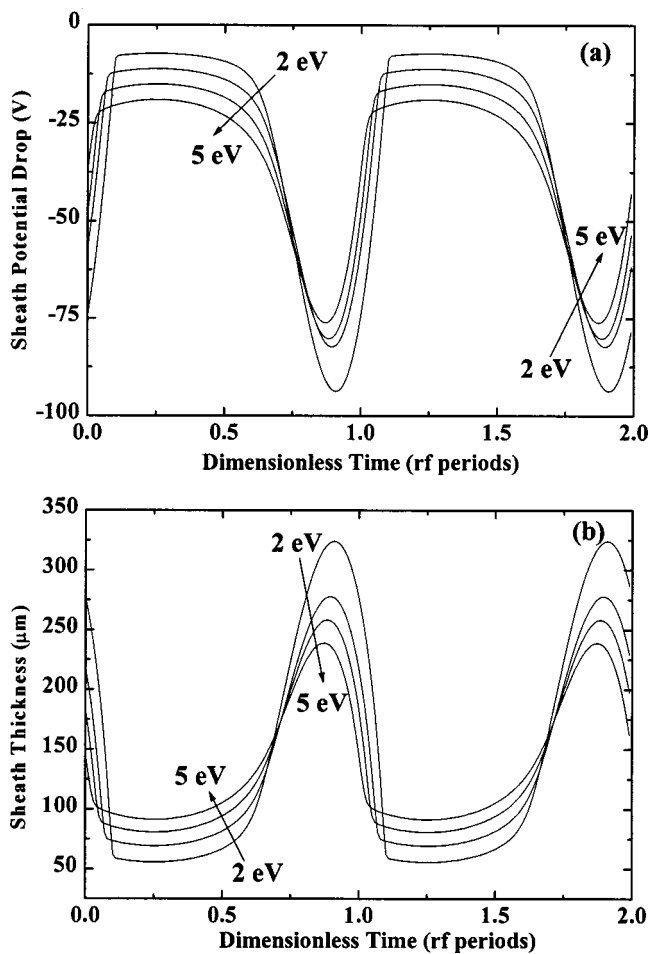


FIG. 12. Effect of the electron temperature on the time dependent sheath potential and sheath thickness with the rf-bias power and plasma ion density held constant at 80 W and  $3 \times 10^{11} \text{ cm}^{-3}$ , respectively.

Since this difference is proportional to the electron temperature,  $\Delta V_{s,\min}$  increases with electron temperature resulting in the shift of the low energy peak position to higher energies. Figure 12 shows the time dependent sheath potential and the sheath thickness for the values of the electron temperatures in Fig. 11. It is clear from Fig. 12 that the minimum potential difference between the plasma and the electrode is increasing with increasing electron temperature and that the peak-to-peak sheath potential is decreasing. Since the minimum potential drop increases with electron temperature and the applied rf-bias power is held constant at 80 W, the peak-to-peak voltage must decrease to satisfy Eq. (36). As the product of the current and voltage increases during the fraction of the rf cycle when the potential is closest to the floating potential, the product of the current and voltage for the remainder of the rf cycle must decrease.

A second effect of the electron temperature on the IEDs is the change in the ratio of the low and high energy peak heights. As the electron temperature decreases, the ratio of the low energy peak height to the high energy peak height decreases significantly as illustrated in Fig. 11. The effect of decreasing the electron temperature is similar to the effect of increasing the rf-bias power and it can be attributed to the

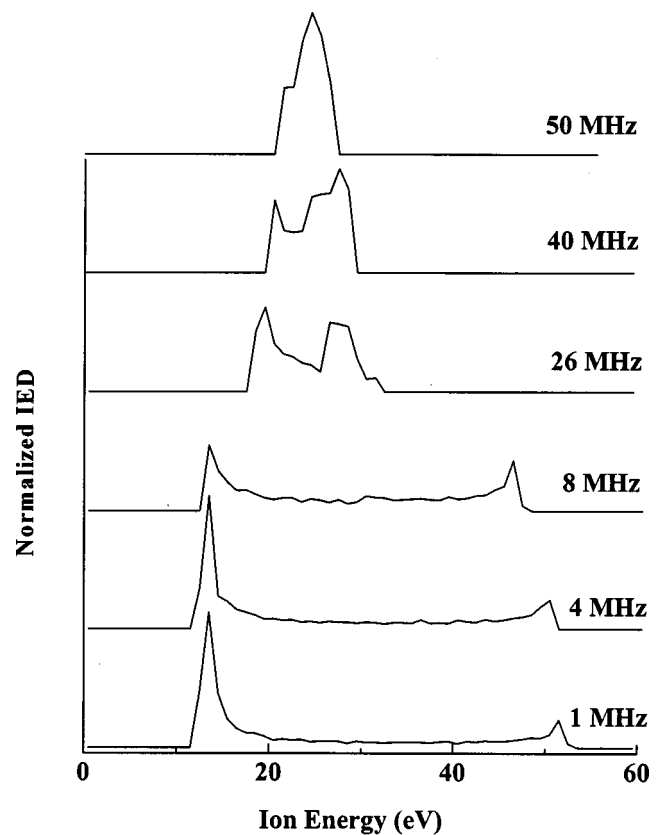


FIG. 13. Effect of frequency on the simulated ion energy distributions. The rf-bias power, electron temperature, ion mass, and ion density are kept constant at 80 W, 3 eV, 40 amu, and  $3 \times 10^{11} \text{ cm}^{-3}$ , respectively. The distributions were shifted upward on the IED axis for clarity.

decreased fraction of time spent when the sheath potential is at its minimum value.

Figure 13 shows the effects of the rf-bias frequency on the simulated IEDs in an Ar plasma with the rf bias, ion density, and electron temperature kept constant at 80 W,  $3 \times 10^{11} \text{ cm}^{-3}$ , and 3 eV, respectively. The effects of frequency on the IEDs can be investigated even though we assumed that the ensemble average of the ion density and the ion velocity follow the temporal variation of the electric field and neglected the time dependent terms in the continuity and ion momentum balance equations. The spatiotemporal variation of the sheath potential (i.e., Poisson's equation) is relatively insensitive to details of the variation of the ensemble average ion density and average velocity with time. The fact that individual ions cannot respond to the field instantaneously at higher frequencies can be taken into account in the Monte Carlo simulations. Ions traversing the sheath when the rf-bias period is long (i.e., low frequency) with respect to the ion transit time across the sheath will have a fully modulated energy distribution. This means that an ion will traverse the sheath before the potential drop changes significantly and will therefore arrive at the electrode with energy equal to the instantaneous potential drop across the sheath at the time the ion entered the sheath. The IED at 1 MHz in Fig. 13 illustrates a fully modulated ion energy distribution. In contrast, ions traversing the sheath at higher rf-bias frequencies will experience several rf cycles before reaching the electrode. At

higher frequencies, ions will impinge on the electrode with energy equal to the average potential drop across the sheath regardless of the moment in the rf cycle that they enter the sheath. Thus at high enough frequencies (e.g., IED simulated at 50 MHz in Fig. 13) the IEDs will exhibit a single peak at the average sheath potential drop.

## B. Comparisons with experiments

Ion energy distribution functions were measured in a Lam TCP plasma reactor at various TCP coil and rf-bias powers in both Ar and Ne discharges. The rf-bias power, the ion density at the plasma-sheath interface, and the electron temperature in the plasma are inputs to the model. Thus, if the ion density at the plasma-sheath interface and the electron temperature are known, one can compare the measured IEDs to the simulated IEDs. Experimentally, changing the rf power to the TCP coil varies the ion density in the plasma volume at constant rf bias. It is very difficult to measure the ion density at the plasma-sheath boundary without disturbing the sheath. The electron temperature and the ion density measured using a Langmuir probe 6 cm above the electrostatic chuck were used as guidelines in choosing  $n_i$  and  $kT_e$  for the model when comparing simulated and measured IEDs. Thus, the model does not contain any arbitrarily adjustable parameters and we are constrained in our choices for the values for  $n_i$  and  $kT_e$  by the Langmuir probe measurements.

### 1. Comparisons as a function of the rf-bias power

Experimentally measured and simulated IEDs are compared in Fig. 14 as a function of the rf-bias power in an Ar plasma. Figure 14(a) shows the measured IEDs in an Ar plasma at 10 mTorr maintained with 700 W TCP coil power as a function of rf-bias power between 40 and 100 W. Figure 14(b) shows the simulated IEDs in an Ar plasma using an ion density of  $3 \times 10^{11} \text{ cm}^{-3}$  and an electron temperature of 3 eV. The ion density has been shown to remain constant with increasing rf-bias power when the TCP coil power is much larger than the rf-bias power.<sup>23</sup> Thus, at low enough rf-bias powers, the sole effect of the rf bias is to change the sheath potential drop without significantly affecting the plasma generated and maintained by the TCP coil. For this reason we kept the ion density and electron temperature inputs to the model constant as a function of the rf-bias power. The peak rf current,  $I_{\text{max}}$ , was chosen such that the calculated rf-bias power was close to the experimentally set rf-bias power. Under these conditions the measured ion density in the plasma was  $2.1 \times 10^{11} \text{ cm}^{-3}$  and the electron temperature was 3.0 eV. We could obtain similar agreement between the simulated and measured IEDs by choosing  $n_i = 2.1 \times 10^{11} \text{ cm}^{-3}$  and increasing  $kT_e$  slightly but such minor adjustments are within the experimental error of the Langmuir probe measurements, rf power measurements, and the accuracy expected from the model. Since it is difficult to set and measure the boundary conditions at the plasma-sheath interface, we simply opted for choosing  $n_i$  and  $kT_e$  consistent with the Langmuir probe measurements without attempting to fit the data exactly.

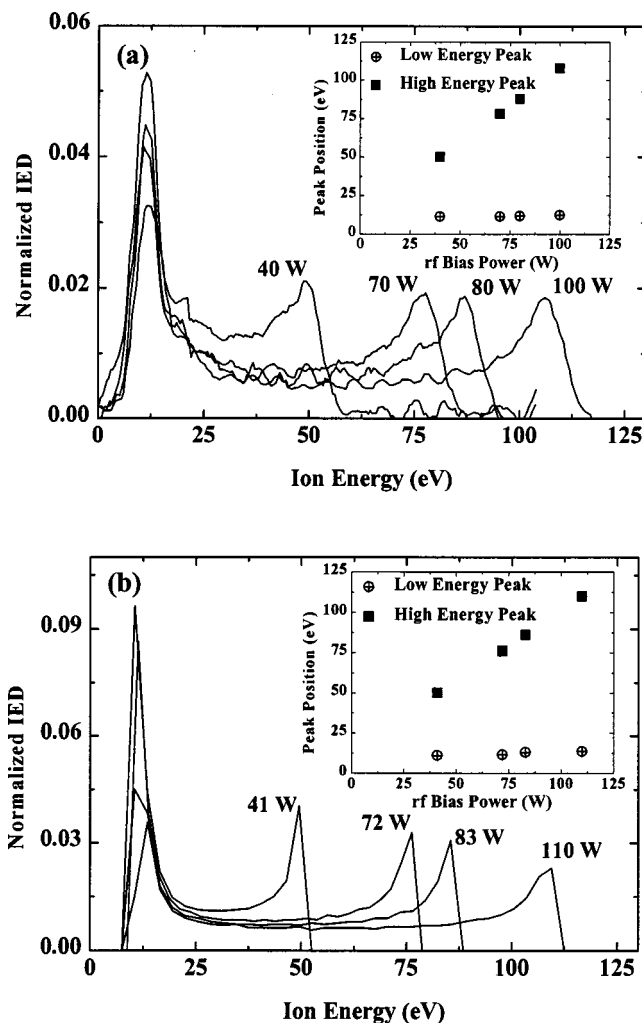


FIG. 14. Comparison of (a) experimentally measured IEDs in an Ar plasma maintained at 700 W TCP power and 10 mTorr with (b) simulated Ar IEDs with ion densities and electron temperatures of  $3 \times 10^{11} \text{ cm}^{-3}$  and 3 eV, respectively, for various rf-bias powers. Under the experimental conditions of (a) the ion density and the electron temperature were measured to be  $2.1 \times 10^{11} \text{ cm}^{-3}$  and 3 eV, respectively. The inset shows the position in energy of the high and low energy peaks of the bimodal distributions as a function of the rf-bias power.

The scaling of peak positions with rf bias and the ratio of the low energy peak height to the high energy peak height in the experiments are captured by the model and match the experimental results. The absolute value of the measured and simulated peak heights do not match for two reasons. First, the experimental peaks are slightly broader than the simulated peaks. Second, small errors in the experimentally measured IED in the region between the two peaks result in a large error in the total integrated area, particularly when the peaks are separated by a large energy. Since normalization involves division of the IED by the total integrated area, this error propagates to the absolute peak heights. For this reason we use the peak positions and the relative ratio of peak heights for the comparison with the model predictions. In Fig. 14, the ratio of the measured and simulated low energy peak heights to the high energy peak heights are 2.6 and 2.5, respectively, at 40 W. At 100 W these ratios are 1.5 and 1.6 for the measured and simulated IEDs, respectively.



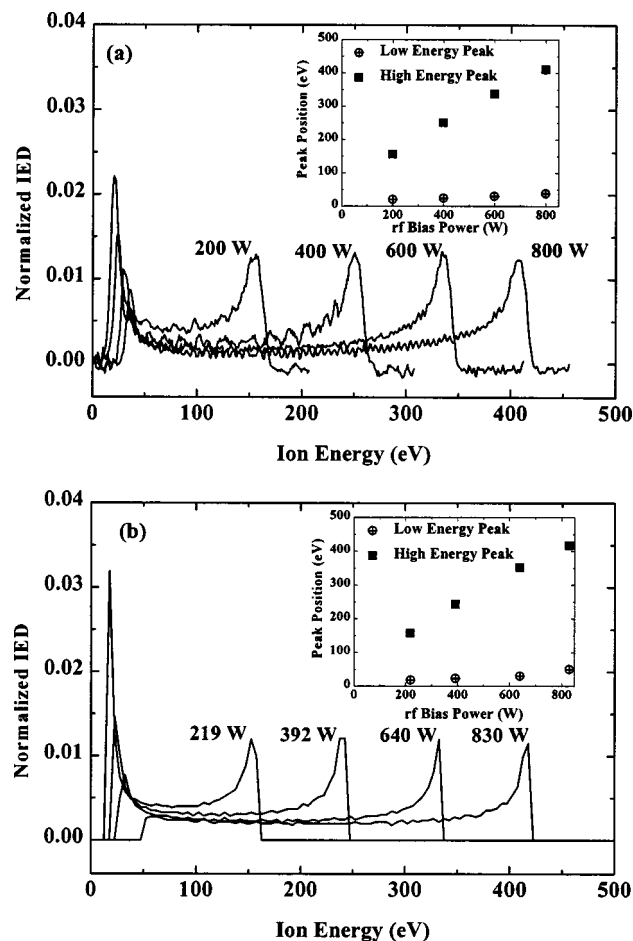


FIG. 15. Comparison of (a) experimentally measured IEDs in an Ar plasma maintained at 1500 W TCP power and 10 mTorr with (b) simulated Ar IEDs for high rf-bias powers between 200 and 800 W. The electron temperatures of the simulated IEDs were changed from 3.5 eV at 219 W to 5.0 eV at 830 W to account for the experimentally measured shift in the low energy peak of the IEDs with increasing rf-bias power. The inset shows the position in energy of the high and low energy peaks of the bimodal distributions as a function of the rf-bias power.

The ion energy distributions in an Ar plasma at 5 mTorr and 1500 W of TCP coil power were measured with 200–800 W rf bias applied to the electrode and are shown in Fig. 15(a). Figure 15(b) shows the simulated IEDs corresponding to the data shown in Fig. 15(a). As the rf-bias power is increased, the low energy peak height becomes smaller than the high energy peak height. At high rf-bias power the sheath becomes so thick that the ions that start traversing the sheath when the electrode potential is closest to the plasma potential do not make it to the electrode before the potential increases. These ions are accelerated to higher energies and fewer ions arrive at the electrode with low energies. A more subtle effect of the rf-bias power is the shift in the low energy peak to higher energies with increasing rf-bias power. In order to simulate this shift in the low energy peak we chose different values of  $kT_e$  for each of the rf-bias powers. For the 219 W simulation we used a  $kT_e$  of 3.5 eV and in the 830 W simulation we used a  $kT_e$  of 5.0 eV. Langmuir probe data were not available for these experiments and the values of  $kT_e$  we used were simply the best fits to the measurements. The ion densities used in the simulations were  $3.5 \times 10^{11} \text{ cm}^{-3}$  for the

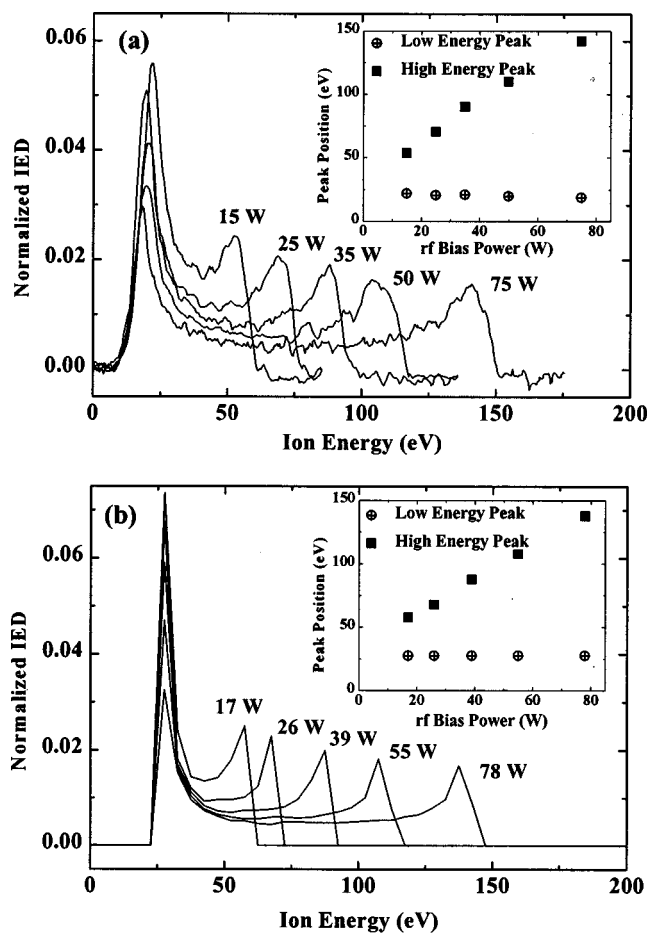


FIG. 16. Comparison of (a) experimentally measured IEDs in a Ne plasma maintained at 1000 W TCP power and 10 mTorr with (b) simulated Ne IEDs with ion densities and electron temperatures of  $7.5 \times 10^{10} \text{ cm}^{-3}$  and 6.5 eV, respectively, for various rf-bias powers. Under the conditions of (a) the measured ion density and electron temperature are  $6.5 \times 10^{10} \text{ cm}^{-3}$  and 6.5 eV, respectively. The inset shows the position in energy of the high and low energy peaks of the bimodal distributions as a function of the rf-bias power.

200 and 400 W data and  $3.8 \times 10^{11} \text{ cm}^{-3}$  for the 600 and 800 W data. A slight increase in ion density may be expected with increasing rf bias, particularly at high power, since some power will go into ionization in addition to accelerating the ions. Remarkably, the choices of  $n_i$  between  $3.5 \times 10^{11}$  and  $3.8 \times 10^{11} \text{ cm}^{-3}$  and of  $kT_e$  between 3.5 and 5 eV lead to excellent agreement between the measured and simulated IEDs.

Figure 16(a) shows the IEDs measured in a Ne plasma at 10 mTorr and 1000 W TCP power for rf-bias powers between 15 and 75 W. The ion density measured was  $6.3 \times 10^{10} \text{ cm}^{-3}$  and the electron temperature measured was 6.5 eV. Figure 16(b) shows the simulated IEDs for a Ne plasma using an ion density of  $7.5 \times 10^{10} \text{ cm}^{-3}$  and an electron temperature of 6.5 eV. The model accurately predicts the peak positions and the steady decrease in the peak heights as a function of the rf-bias power.

## 2. Comparisons as a function of the TCP coil power

The effects of the TCP coil power on the ion energy distributions with the reactor pressure and the chuck bias

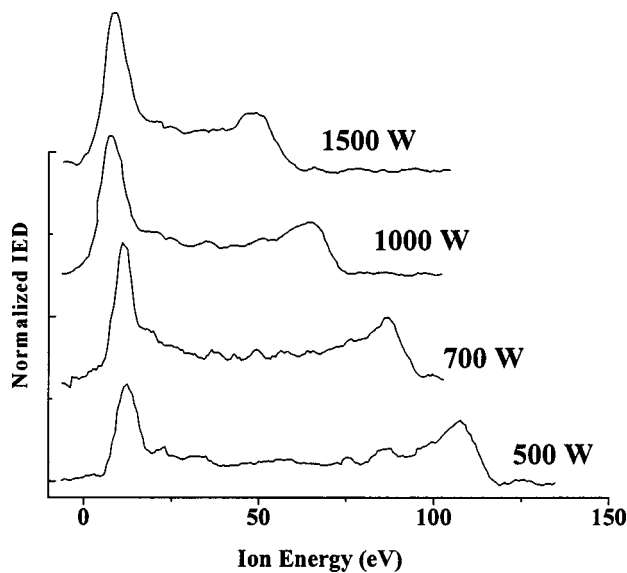


FIG. 17. Experimentally measured IEDs in an argon plasma as a function of TCP power between 500 and 1500 W. The rf-bias power was kept constant at 80 W and the pressure was 10 mTorr. These measured IEDs should be compared with the simulated IEDs in Fig. 9 which shows the effect of ion density on the IEDs. Changing the TCP power has the effect of changing the plasma density.

maintained at 5 mTorr and 80 W, respectively, are shown in Fig. 17. The ion density in the plasma and therefore the current flux to the electrode increases with increasing TCP power. The simulated energy distributions with constant  $kT_e$  and rf-bias power and varying ion density were discussed earlier and are illustrated in Fig. 9. Figure 17 shows the experimentally measured IEDs which should be compared with the simulations shown in Fig. 9. The change in the TCP coil power was simulated by changing the plasma ion density in the model. The effects of ion density on the peak-to-peak voltage of the electrode were discussed in Sec. IV A. In order to keep the time-averaged rf-bias power constant, the peak-to-peak voltage on the chuck must decrease as the current increases. This decrease in peak-to-peak electrode potential is manifested as the shift in the high energy peak of the IED measured towards lower energies, shown in Fig. 17.

The ion densities measured using a Langmuir probe and the ion densities used to simulate the measurements are shown in Fig. 18. Although the values are not exactly the same, the differences between the simulated and measured ion densities are within a factor of 2. Both the measured ion densities and the ion densities used to simulate the measured IEDs have an approximately linear relationship. The difference between the simulated values and the measured values is probably within the accuracy of the Langmuir probe measurements.

## V. CONCLUSIONS

A hybrid model of a collisionless rf modulated sheath in a high density plasma has been developed for calculating the energy distribution of ions impinging on a rf-biased electrode. The spatial distribution of the time dependent electric

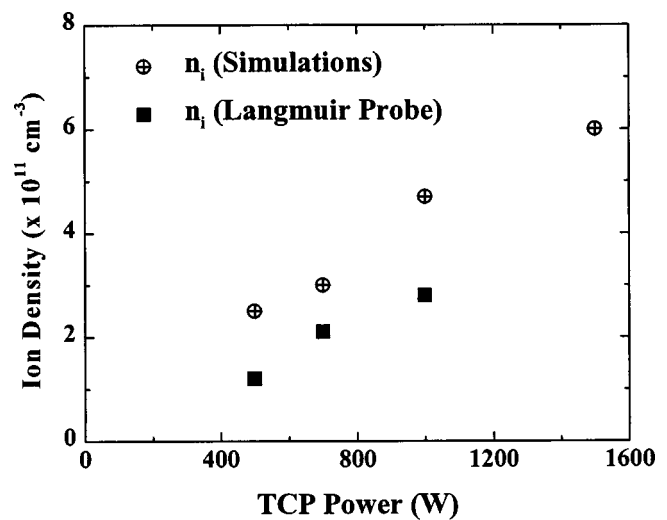


FIG. 18. Comparison of (a) experimentally measured ion densities using a Langmuir probe under the same conditions as the experiments shown in Fig. 17 with (b) the ion densities used to model the IEDs simulated in Fig. 9.

field in the sheath is calculated by assuming that the spatial distribution of the average ion density and average ion drift velocity respond to the time dependent potential instantaneously. However, ion inertia was taken into account in the Monte Carlo simulations of ion trajectories determined by the time dependent electric fields calculated from the sheath model. The calculated ion energy distributions are bimodal, with a low energy peak and a high energy peak. The low energy peak position is a function of the electron temperature and the ion mass and is therefore independent of the rf-bias power. The high energy peak scales linearly with increasing rf-bias power to higher energies. The ratio of the peak heights for low rf-bias powers is such that the majority of ions arrive at the electrode with low energies. As the rf-bias power increases there is an inversion in peak heights and at high enough rf bias the majority of the ions arrive with high energies. The effects of ion density, electron temperature, and rf-bias frequency have been investigated. Measurements of ion energies at a rf-biased electrostatic chuck in a Lam TCP reactor were performed and compared with the simulations and showed good agreement with the experimental results. The model accurately predicts both the peak positions and the peak heights under various operating conditions for both Ar and Ne plasmas.

## ACKNOWLEDGMENTS

This work was funded by Lam Research Corporation and by the National Science Foundation National Young Investigator Program (Award No. ECS 9457758). The authors would like to thank Dr. Andrew Perry, Dr. Neil Benjamin, Dr. Richard Gottscho, and Dr. Vahid Vahedi of Lam Research Corporation for their contributions to the design of the ion energy analyzer and for fruitful discussions during this project. Dr. Perry and Dr. Benjamin were instrumental in the design of the ion energy analyzer (IEA) and in the ion energy distribution (IED) measurements made in the TCP reactor.

- <sup>1</sup>J. Hopwood, *Plasma Sources Sci. Technol.* **1**, 109 (1992).
- <sup>2</sup>M. A. Lieberman and R. A. Gottscho, in *Thin Films*, edited by M. Francombe and J. Vossen (Academic, Orlando, FL, 1993).
- <sup>3</sup>J. P. Chang, J. C. Arnold, G. C. H. Zau, H.-S. Shin, and H. H. Sawin, *J. Vac. Sci. Technol. A* **15**, 1853 (1997).
- <sup>4</sup>A. Metze, D. W. Ernie, and H. J. Oskam, *J. Appl. Phys.* **60**, 3081 (1986).
- <sup>5</sup>D. J. Economou, D. R. Evans, and R. C. Alkire, *J. Electrochem. Soc.* **135**, 756 (1988).
- <sup>6</sup>M. A. Lieberman, *IEEE Trans. Plasma Sci.* **16**, 638 (1988).
- <sup>7</sup>M. A. Lieberman, *IEEE Trans. Plasma Sci.* **17**, 338 (1989).
- <sup>8</sup>V. A. Godyak and N. Sternberg, *IEEE Trans. Plasma Sci.* **18**, 159 (1990).
- <sup>9</sup>V. A. Godyak and N. Sternberg, *Phys. Rev. A* **42**, 2299 (1990).
- <sup>10</sup>K. Bornig, *Appl. Phys. Lett.* **60**, 1553 (1992).
- <sup>11</sup>V. A. Godyak, R. B. Piejak, and N. Sternberg, *IEEE Trans. Plasma Sci.* **21**, 378 (1993).
- <sup>12</sup>N. Sternberg and V. A. Godyak, *IEEE Trans. Magn.* **30**, 3100 (1994).
- <sup>13</sup>M. J. Grapperhaus and M. J. Kushner, *J. Appl. Phys.* **81**, 569 (1997).
- <sup>14</sup>P. A. Miller and M. E. Riley, *J. Appl. Phys.* **82**, 3689 (1997).
- <sup>15</sup>R. T. C. Tsui, *Phys. Rev.* **168**, 107 (1967).
- <sup>16</sup>R. H. Bruce, *J. Appl. Phys.* **52**, 7064 (1981).
- <sup>17</sup>M. J. Kushner, *J. Appl. Phys.* **58**, 4024 (1985).
- <sup>18</sup>G. A. Hebner and M. J. Kushner, *J. Appl. Phys.* **62**, 2256 (1987).
- <sup>19</sup>A. Metze, D. W. Ernie, and H. J. Oskam, *J. Appl. Phys.* **65**, 993 (1989).
- <sup>20</sup>M. S. Barnes, J. C. Forster, and J. H. Keller, *IEEE Trans. Plasma Sci.* **19**, 240 (1991).
- <sup>21</sup>R. J. Hoekstra and M. J. Kushner, *J. Appl. Phys.* **79**, 2275 (1996).
- <sup>22</sup>P. Benoit-Cattin and L. C. Bernard, *J. Appl. Phys.* **39**, 5723 (1969).
- <sup>23</sup>E. A. Edelberg, A. J. Perry, N. Benjamin, and E. S. Aydil, *J. Vac. Sci. Technol. A* **17**, 506 (1999).
- <sup>24</sup>E. A. Edelberg, A. J. Perry, N. Benjamin, and E. S. Aydil, *Rev. Sci. Instrum.* (1999).
- <sup>25</sup>R. A. Gottscho, *J. Vac. Sci. Technol. B* **11**, 1884 (1993).